

MELT POOL FEATURE EXTRACTION, SPATIAL REGISTRATION, AND LAYER-TO-LAYER CONTROL IN POWDER BED FUSION

Bumsoo Park[†], Xin Wang^{††}, Sandipan Mishra[†], Douglas Bristow^{††}, and Robert Landers^{†††}

[†]Mechanical, Aerospace, and Nuclear Engineering, Rensselaer Polytechnic Institute, Troy, NY 12180

^{††}Mechanical and Aerospace Engineering, Missouri University of Science and Technology, Rolla, MO 65409

^{†††}Aerospace and Mechanical Engineering, University of Notre Dame, Notre Dame, IN 46556

Abstract

Laser Powder Bed Fusion (LPBF) is a well-known additive manufacturing technique that uses a high-power laser to fuse loose metal powder into a solid part. A major issue restricting this technology from wider industrial applications is the lack of part quality assurance. In this paper, a high-speed (2kHz) co-axial near-infrared optical camera setup is implemented for process monitoring and control. The acquisition locations for individual images are estimated based on specified scan paths and scan velocities to create a spatial registration technique. Melt pool thermal features are linked to specific locations instead of time instants, motivating a spatial control strategy to achieve thermal feature uniformity. Based on the spatial mapping of the thermal features, experimental studies are conducted where a spatial layer-to-layer iterative learning controller is implemented to achieve spatial uniformity of the thermal features. The experimental results present a convergence of the thermal features to a uniform level.

Introduction

Powder Bed Fusion (PBF) is a powder-bed additive manufacturing technique where a laser beam or an electron beam fuses metal powder layer by layer from a sliced 3D model and produces a solid part. The attraction of PBF comes from its capability to manufacture complex customized geometries with low waste. In the growing markets related to additive manufacturing [1], however, one challenge which prevents it from wider industrial production is the lack of quality control, especially for complex geometries [2]. Therefore, defect diagnosis and melt pool control are active topics in the research of PBF.

Additive manufacturing researchers have explored in-process monitoring tools to overcome the problems of porosity, cracking, thermal management, etc. [3]. In the early work of Berumen et al. [4], an inline process control system was developed for a laser PBF system with photo diodes and an infrared camera. Kruth [4]-[7] et al. conducted a series of experiments using a thermal camera to monitor defects, and implemented Proportional-Integral-Derivative (PID) control with melt pool size and radiation signals. Schwerdtfeger et al. [8] used an infrared camera for in-situ flaw detection in an electron beam PBF system. Demir et al. [9] used optical sensors with multiple channels of bandwidths to record temporal signals of image radiation and its statistics. Shkoruta et al. [10-11] used IR camera measurements for iterative learning control and for frequency-domain analysis. While researchers have monitored, controlled, and identified dynamics in the temporal domain with progress, temporal-domain control has the following challenges:

1. In real applications, thermal cameras generate large data streams, which consume substantial computation resources and cause a delay in control systems. When a camera frame is finished processing, the laser already is processing material several mm away from the point where the frame was obtained, introducing a substantial delay and making real-time control difficult.
2. Defects depend on locations in a geometry instead of time, especially in cases where varying laser paths change the time-location relationship for each layer or cases where the continuity of time is broken when multiple parts with different heights are printed during the same build.

Additive manufacturing researchers made much effort in 3D melt pool thermal feature reconstruction from infrared videos. Krauss et al. [12-13] presented a detailed work on visualized spatial feature maps of melt pool

features in PBF, helping to identify local defects. Lough et al. [14-15] correlated visualized 3D melt pool features to laser parameters and engineering properties.

In this paper, a spatial monitoring and control framework is presented. A high-speed near infrared (NIR) camera is used to monitor melt pools in a PBF platform with CoCr powder. Each camera picture is recorded with a time stamp, and spatial location registration is performed by correlating the time stamps with path information. A simple geometry is presented to show the spatial non-uniformity of melt pool sizes in an open-loop experiment. A spatial ILC algorithm is then applied to regulate the melt pool sizes to a uniform level. A non-uniform pattern that can be seen in this process is the difference between inner points and edge points where paths and thermal boundary conditions are different. The open-loop and closed-loop experimental results show that the spatial controller eliminates the negative effect from the edges and diminishes statistical differences between inner points and edge points.

System description and problem formulation

All experiments presented in this work are performed on an open-architecture PBF machine (Figure 1). The machine is capable of printing on a 50mm×50mm build plate with metal powder such as stainless steel or Inconel, and is equipped with a SCANLAB intelliSCAN 20 galvoscanner and a 400 W NdYAG laser. High-level controls are implemented via AmericaMakes software augmented with C++ codes for custom functionality, whereas low-level machine commands are controlled through the scanner control board, e.g., laser path execution and powder placement. Scan commands for each layer are provided to the machine through a scan file. The scan file is formatted as an xml file containing a list of straight scan lines. Each line is represented in terms of the start and end coordinates, as well as the scan velocity and laser power. While the scan geometry and parameters are typically pre-determined, the laser power can be overwritten at each timestep through high-level control commands.

The PBF system is equipped with a coaxial optical monitoring setup with an NIR filter, capturing images of melt pools during the process. All images in this work are acquired at 2kHz, with a size of 64×64 pixels. The images are represented as a grayscale image, where each pixel provides an intensity value ranging from 0 to 255.

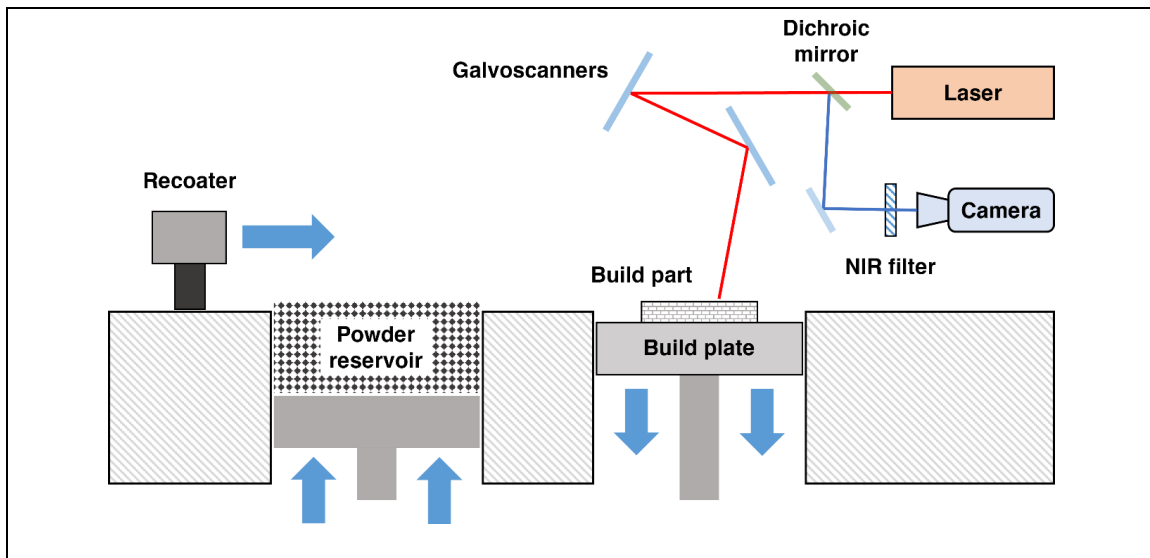


Figure 1: Schematic of PBF testbed and coaxial camera setup.

The objective of this work is to provide a layer-wise spatial control strategy that can compensate for local inhomogeneities in heating due to build-part geometry. We consider the system described above where coaxial measurements are provided without temporal registration. Because spatial/temporal information of each acquired coaxial image is not provided, the images must first be spatially mapped to implement a spatial control algorithm. Additionally, the coaxial images are inherently high-dimensional, making it difficult to directly use for control purposes. Thus, signature extraction from the images must be implemented for dimension reduction purposes,

prior to using the images for control. Once appropriate signatures are extracted from the coaxial images and spatially mapped, these spatially mapped signatures are used to determine the power profile of the subsequent layer.

Methods

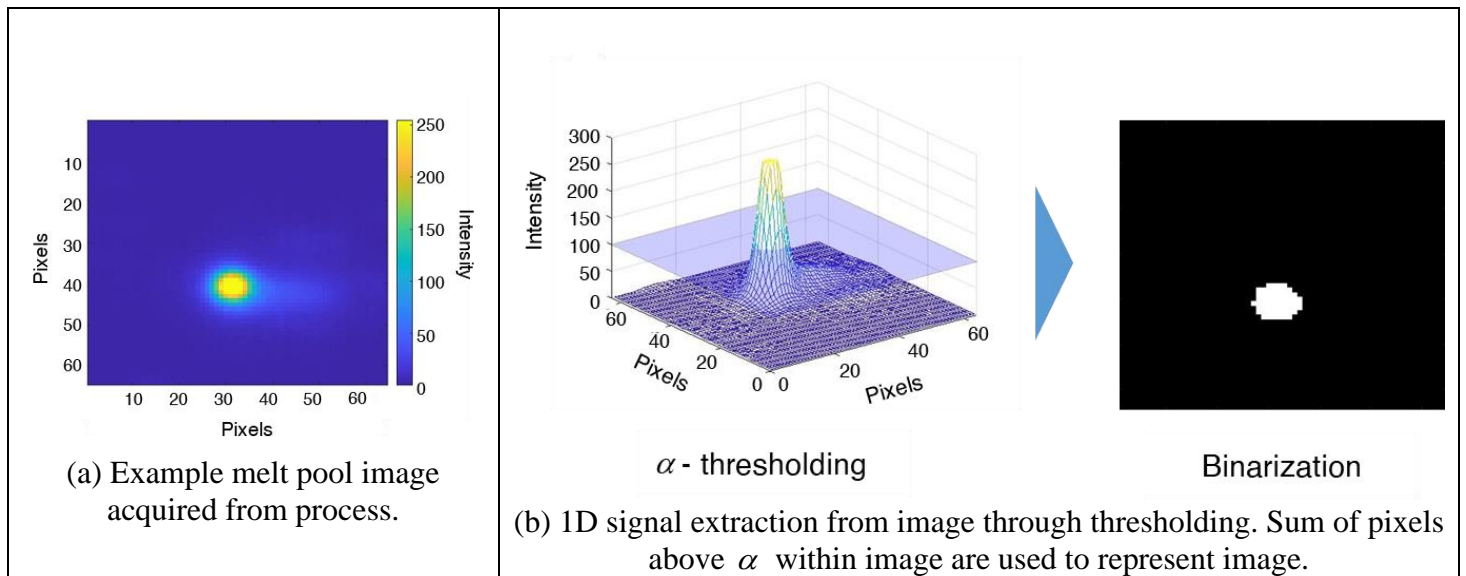


Figure 2: Example melt pool image and signature extraction method.

We first extract a signature from each image to reduce the amount of data that must be stored. Among the various types of available signatures, we use an index proportional to the area of the bright center of the isotherm, as shown in Figure 2 (a). The area index C_α for a given image I is defined as

$$C_\alpha = \sum_{r,c} f(I(r,c) \geq \alpha), \quad (1)$$

where r and c are row and column indices within the image, $I(r, c)$ is the pixel intensity at the coordinate (r, c) , $\alpha \in (0, 255)$ is the threshold value, and $f(\cdot)$ is an indicator function that is equal to 1 if the argument is true, and 0 otherwise.

Different α values represent different aspects of the image. For $\alpha = 1$, the total footprint of the melt pool emission within the image is measured. C_1 is generally more susceptible to noise as effects such as spattering is captured; however, it provides a quantitative index of the total emission and the direction of scan. On the other hand, $\alpha = 100$, represents the brighter region of the melt pool emission, which can be seen as a more accurate representation of the size of the actual melt pool. Hence, in this study we choose $\alpha = 100$, i.e., C_{100} to represent the area of the hot center in the image for process monitoring and control. The images from a layer can then be represented as 1D time signals.

For the 1D coaxial signals, the location of each point is estimated using the following methodology. First, each index is assigned a value in terms of absolute time based on the camera frame rate, i.e., the time with respect to the start of the scan. This results in a timestamp for each individual measurement. After the temporal registration of the measurements, we then use the nominal scan pattern provided in the xml file. Here we assume constant scanning velocity across each scan line, and perfect trajectory tracking. From the scan file, we can interpolate the individual position of each point from the previously generated time vector. During the interpolation, it is worth noting that the first acquisition of the image does not exactly coincide with the starting coordinate of the laser scan. This delay is compensated in the spatial registration (Figure 3). The value of the delay is empirically determined from experimental data. Once the registration is successfully completed, the 1D signal C_α is transformed from a time series $C_\alpha(t, l)$ into a spatial map $C_\alpha(x, y, l)$, providing a basis for the spatial iterative learning control algorithm. Here, t is the absolute time value, (x, y) are the spatial coordinates, and l is the layer index.

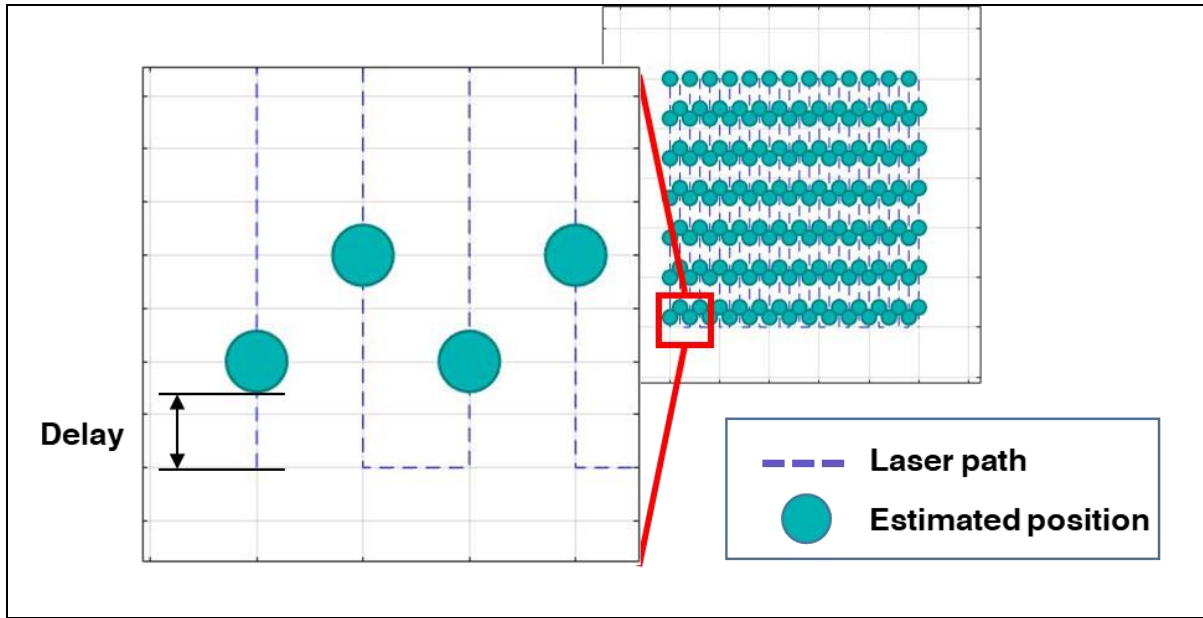


Figure 3: Spatial mapping of 1D coaxial signal with delay compensation

Based on the spatial map of the measurements $C_a(x,y,l)$, an Iterative Learning Control (ILC) algorithm is applied to determine the power profile of the next layer. Depending on the location of (x,y) we first assign a discrete bin value, i.e., voxels which we denote as (x_g,y_g) . We define a power map $P(x_g,y_g,l)$ containing all values of the power commands at the locations (x_g,y_g) in layer l . Given an area index reference value, denoted C_r , the power update for layer $l+1$ is

$$P(x_g, y_g, l+1) = P(x_g, y_g, l) + \gamma e(x_g, y_g, l). \quad (2)$$

where γ is the control gain and e is the spatial error map

$$e(x_g, y_g, l) = C_r - C_a(x_g, y_g, l). \quad (3)$$

Results and discussion

To demonstrate the non-uniformity of melt pool areas, a $2.5 \text{ mm} \times 2.5 \text{ mm} \times 0.9 \text{ mm}$ cuboid was printed (Figure 4). The miniscule geometry was designed to clearly demonstrate spatial-dependent energy accumulation within the build part. Thirty layers in total were printed for all experiments, with a desired layer thickness of 0.03 mm. The scan speed was 800 mm/s with a hatch spacing of 0.1 mm. The optical setup discussed above was then used to track the melt pool during the process at a rate of 2 kHz.

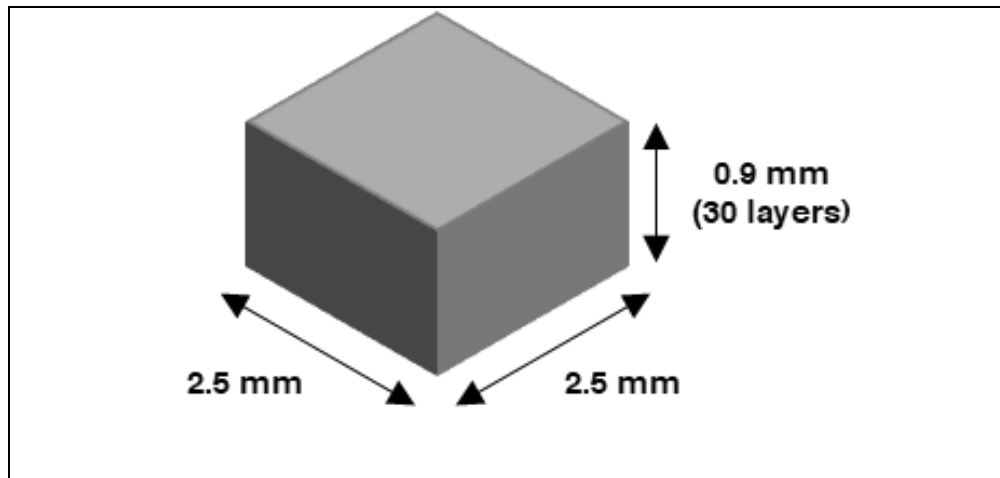
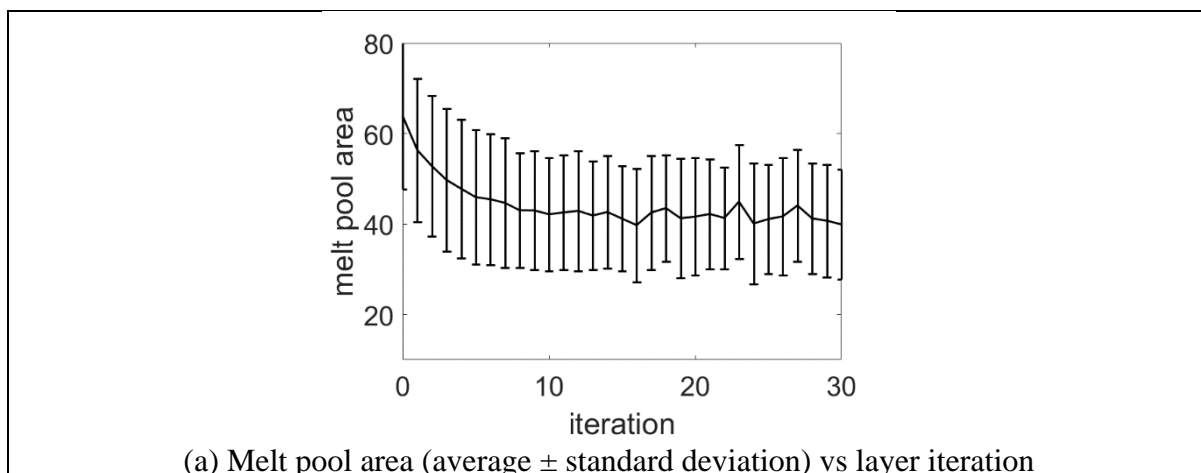


Figure 4: Build part geometry.

We first conducted an open loop test with a constant power of 250 W. We observed transient melt pool behavior during the initial layers of the process. As is shown in Figure 5 (a), the first 10 layers exhibited exponentially decreasing area values and then become relatively constant. This can be attributed to the fact that the layer height is less than $30\ \mu\text{m}$ at the initial layer and gradually increases until it reaches a constant height. As a result, the spatial ILC for closed-loop experiments were all applied after the first 10 layers.

For the open loop test, the spatial registration of $C_{100}(x,y,l)$ is shown in Figure 5 (b), where $l = 30$. The voxel representation of the measurements is shown in Figure 5 (c). While it is possible to have a voxel formulation that contains more than one sample, we chose the voxel size to contain exactly one sample, due to the isometric geometry of the test part. Note that odd columns have 7 measurements and even columns have 6 measurements, creating apparent missing data at the top of the even columns. It can be observed that despite the constant laser power, the measurements are not uniform across the build part, exhibiting geometry-dependent inhomogeneities of the measurements. First, from the spatial signal (Figure 5 (b)), low values on the left and right sides of the layer are noticeable. Second, periodic peaks in measurements appear throughout the layer. This effect is strong at the end of each straight line of the laser path where there is heat accumulation, not only because the loose powder interface creates a heat insulation boundary, but also because the new melt pool absorbs the energy of the previous melt pool when it turns its direction around. There are also random hot spots in the part interior. Figure 5 (c) illustrates a clear alternating pattern between high and low measurements along the upper and lower edges. Figure 6 compares images of the melt pool images before and after a turnaround, depicting a clear difference in the melt pool sizes.



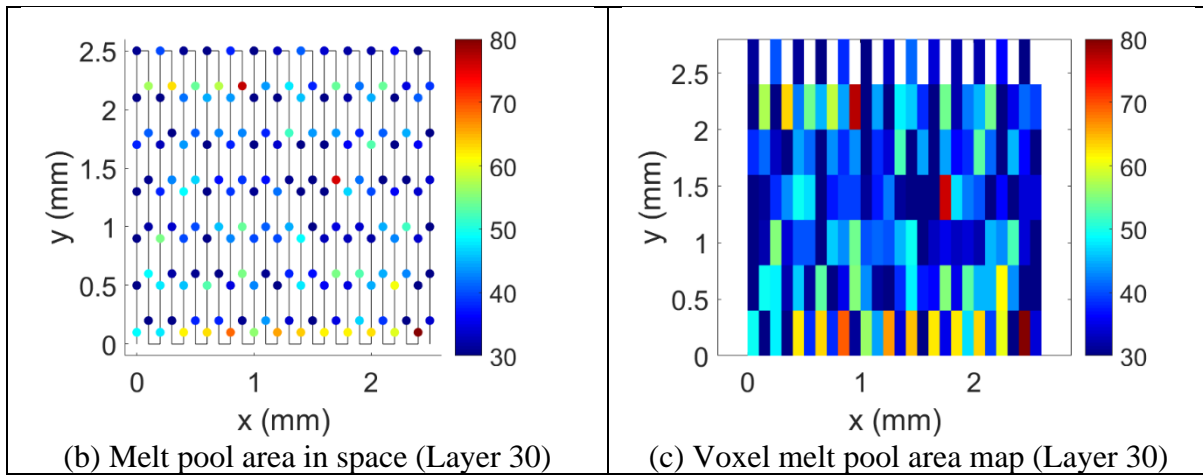


Figure 5: Open-loop experiment data. Dashed line is the reference.

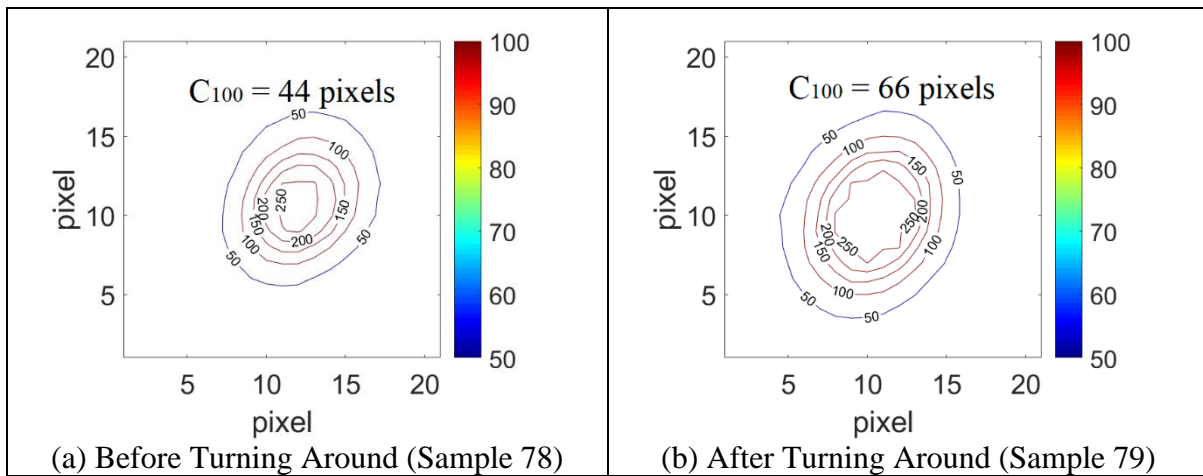
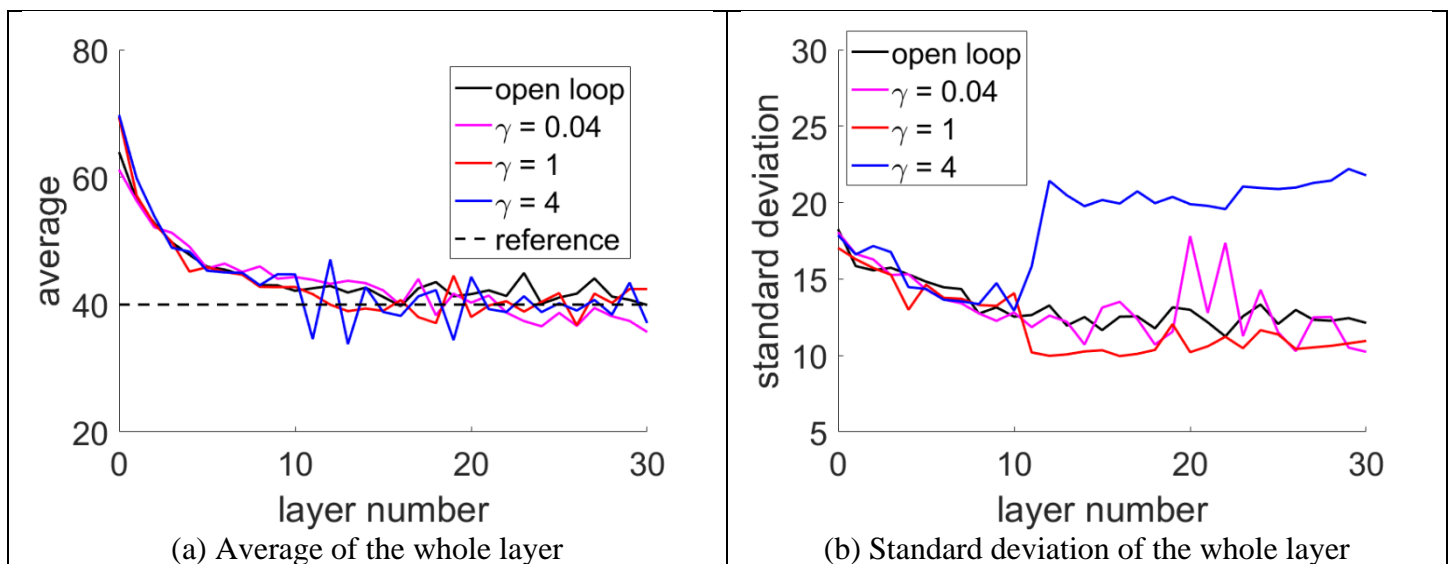


Figure 6: Melt pools before and after path changes direction (open-loop).

To demonstrate the efficacy of the proposed spatial ILC algorithm, we conducted closed-loop experiments with a constant reference value of 40 and control gains $\gamma = 0.04, 1$ and 4 . To avoid the transient behavior of the first several layers affecting the controller, the controller begins after 10 layers.

The averages and standard deviations of the open-loop experiment and the three closed-loop experiments are plotted in Figure 7. Since melt pools have different shapes and sizes in different regions, the statistics of all points, inner points, upper and lower edges, and left and right edges are plotted separately in Figure 7.



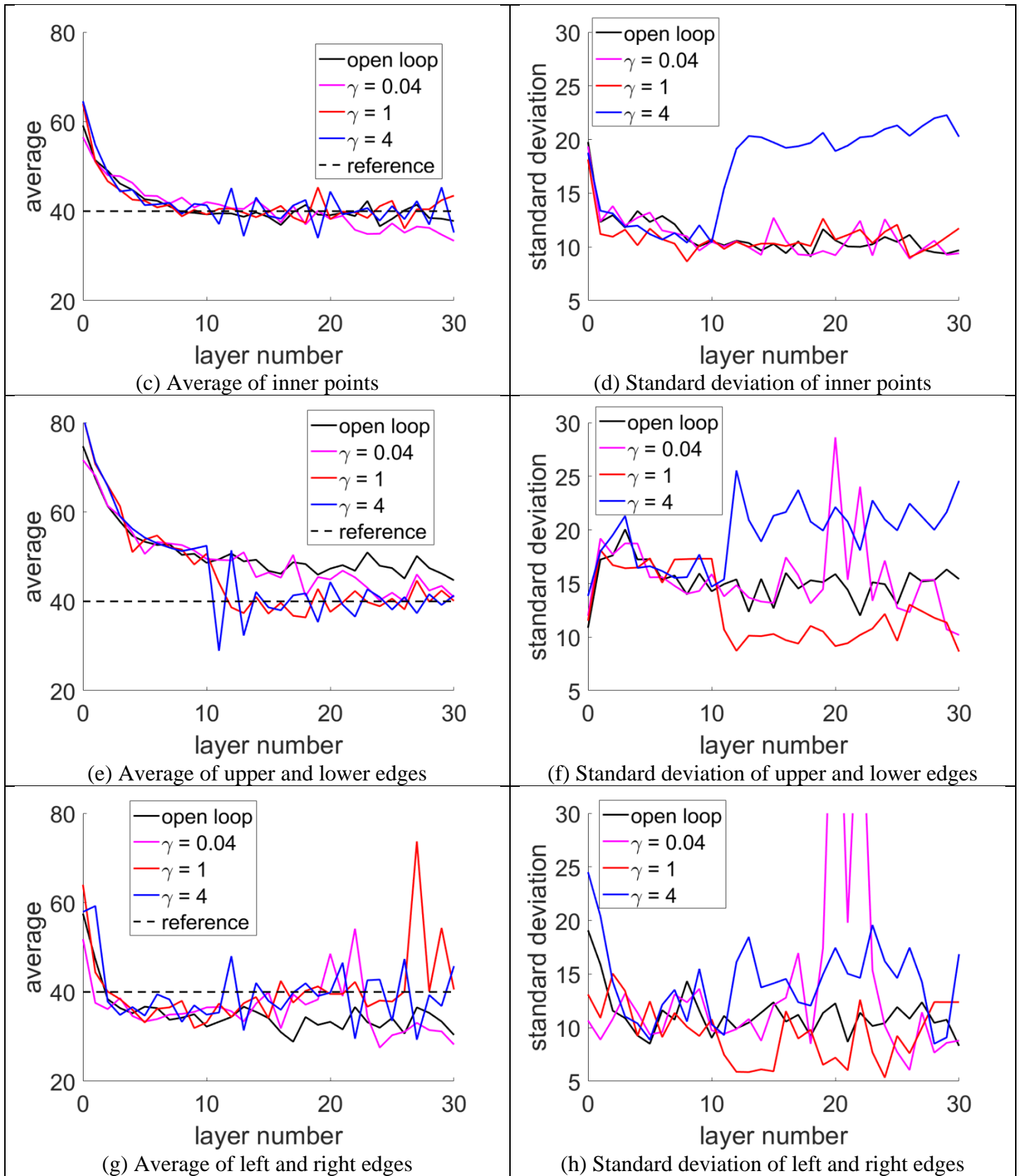


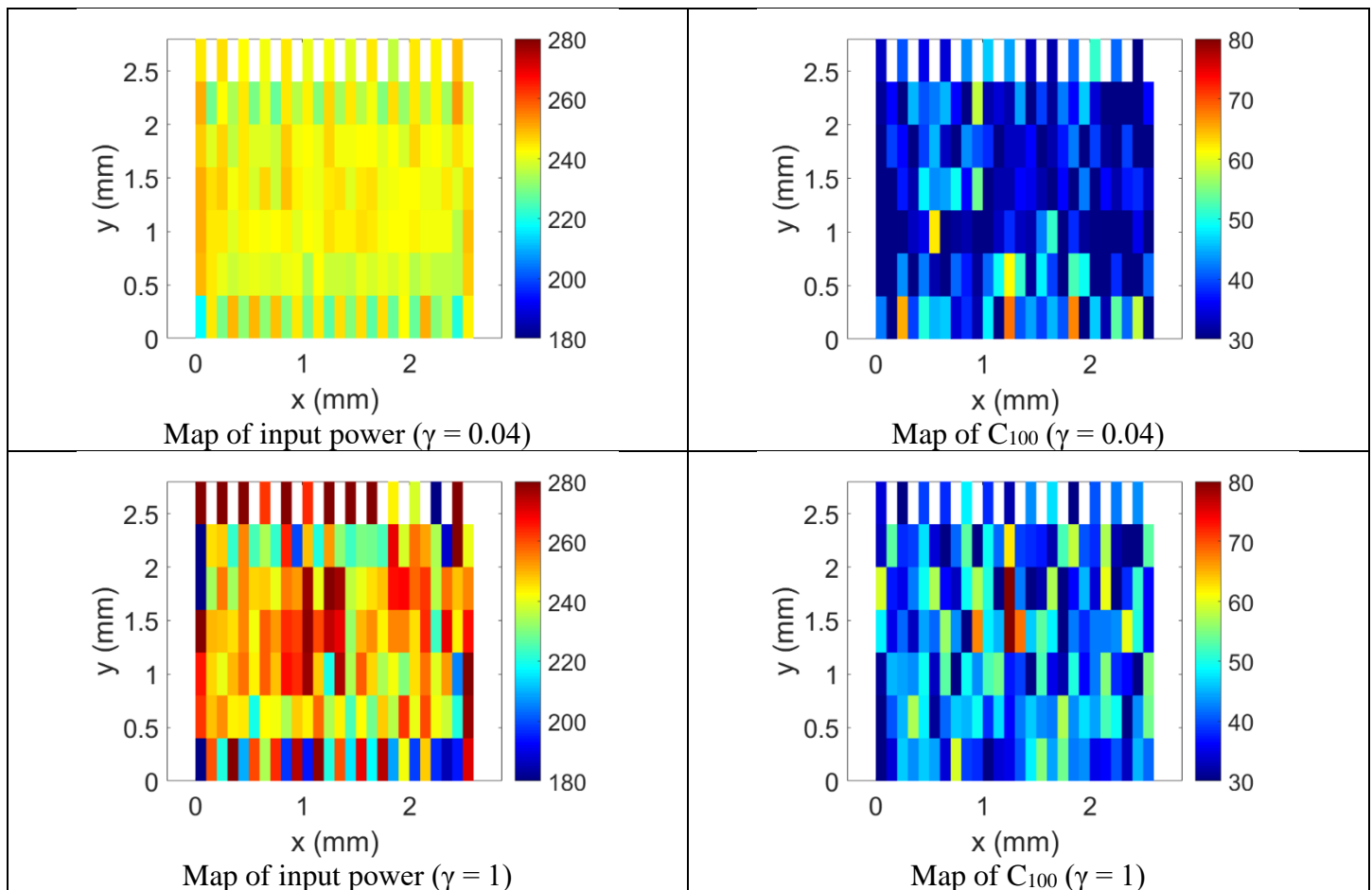
Figure 7: Experiment results of melt pool area over iterations.

For all four regions, the average and standard deviations are almost the same for the open-loop and closed-loop cases for the first ten layers since the controllers do not begin until layer 11. In Figure 7 (a), the open-loop average melt pool area for all of the data converges to a level slightly higher than 40 while the three closed-loop results all converge to approximately 40. The standard deviations for all of the data (Figure 7(b)) are approximately 10 for the controller with $\gamma = 1$, approximately 12.5 for the open-loop and the controller with $\gamma =$

0.04, and 20 for the controller with $\gamma = 4$. The low standard deviation for the controller with $\gamma = 1$ is due to the fact that it is able to regulate the edges better than controllers with other gains. For the controller with $\gamma = 0.04$ there are also disturbances at layers 20 and 22 that are the result of the first pixel having a very large area. The large gain is sensitive to process noise and creates large changes in laser power from layer to layer. The results for the inner points, i.e., Figure 7 (c)(d), illustrate that the larger variation for the open-loop and controller with $\gamma = 0.04$, as compared to the controller with $\gamma = 1$, are due to larger variations on the edges for the open-loop and controller with $\gamma = 0.04$. Again, the controller with $\gamma = 4$ has a greater standard deviation due to the amplification of the process noise.

Figure 7 (e)(f) give the results for the upper and lower edges are where the melt pools turn around and Figure 7 (g)(h) give the results for the left and right edges. While the control experiments are able to regulate the edges to the reference melt pool area, the open-loop melt pool areas are large on the upper and lower edges and small on the left and right part edges. The standard deviations for the controller with $\gamma = 1$ are much smaller than all of the other cases, while standard deviations for the controller with $\gamma = 4$ have the largest standard deviations. The standard deviations are similar for the open-loop and for the controller with $\gamma = 0.04$. Again, there are noticeable disturbances for the controller with $\gamma = 0.04$.

The input maps and output maps of the last layer in the control experiments are plotted in Figure 8. The controller with $\gamma = 0.04$ has less variation in the laser power map as compared to the other controllers; however, the part edges are not regulated as well as the edges of the part using the controller with $\gamma = 1$. The controller with $\gamma = 1$ introduces more variation in the laser power map; however, the entire part is regulated more uniformly than the parts using the other controllers. Again, the controller with $\gamma = 4$ creates input and output maps that have substantial variations.



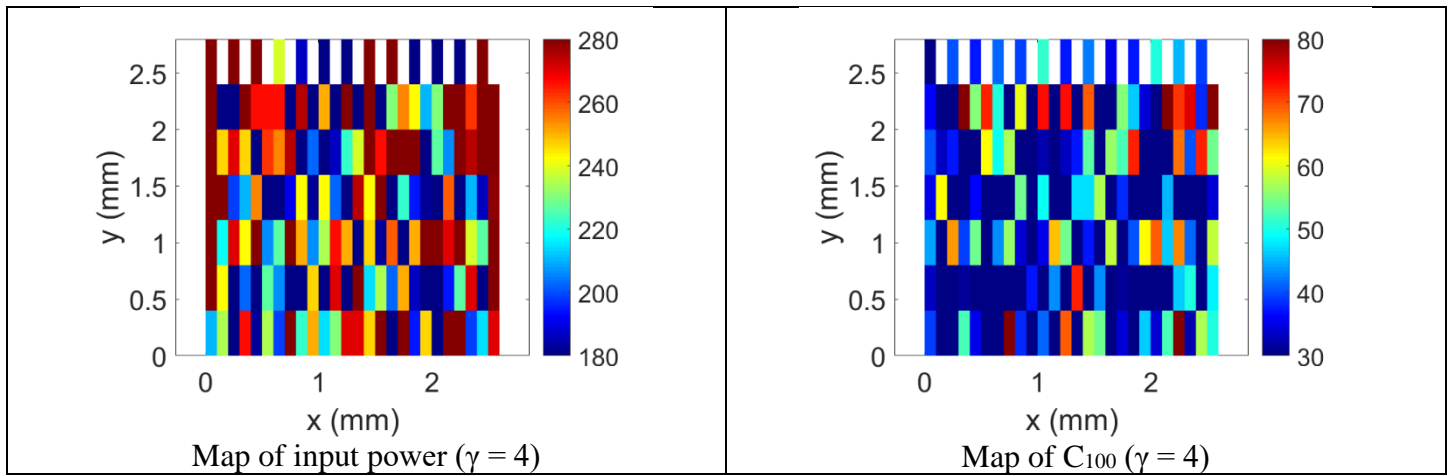


Figure 8: Input power and melt pool area maps at layer 30.

There are single voxels in Figure 7 with very large melt pool areas compared to the surrounding melt pools. For example, in the experiment using the controller with $\gamma = 0.04$, layer 20 has disturbances from large melt pools as shown in Figure 9. There are three examples with different shapes. Example 1 is an abnormal melt pool that is extremely large. Example 2 is normal when the melt pool turns around. Example 3 is a normal melt pool with a tail from the previous melt pool.

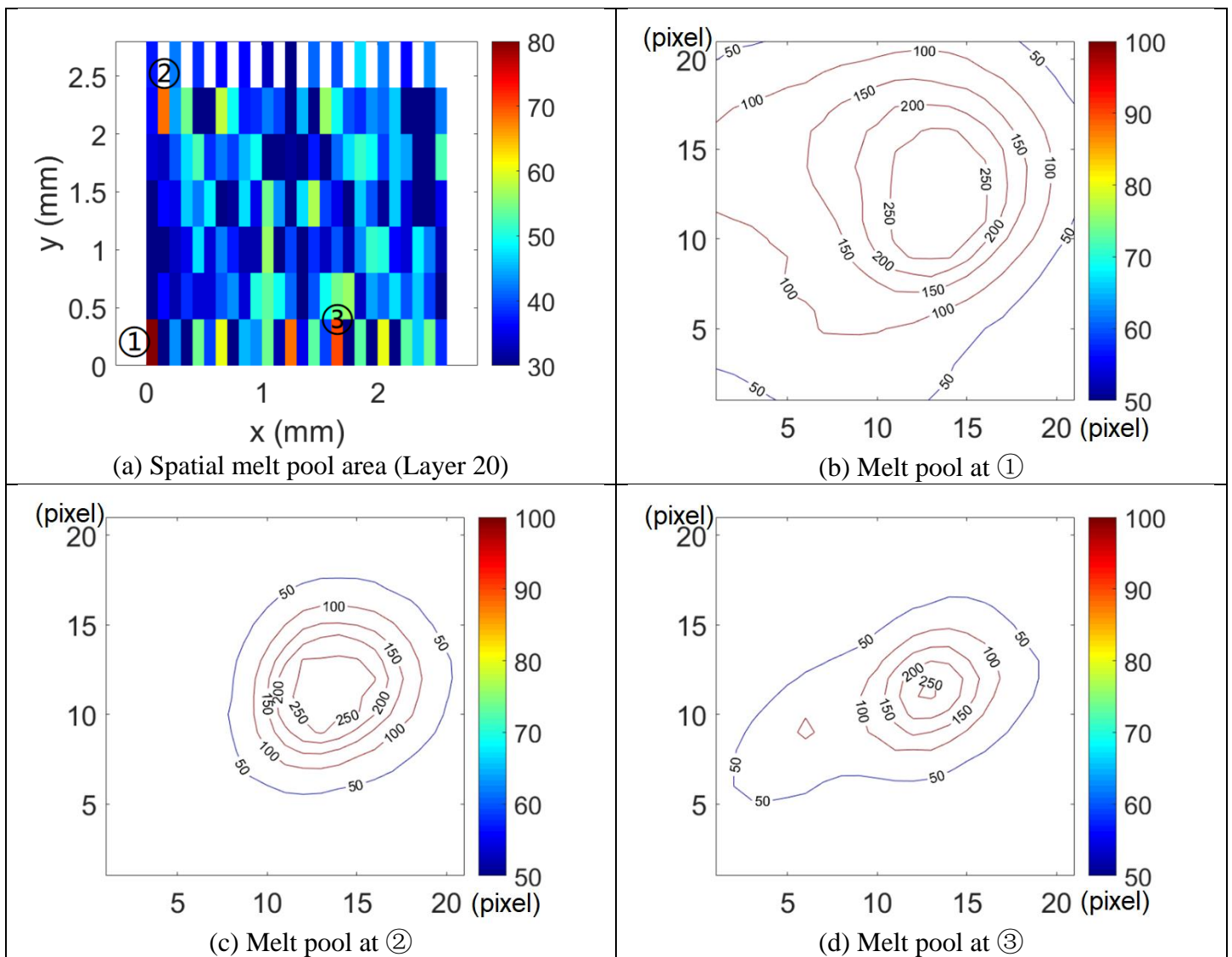


Figure 9: Examples of large melt pools.

Summary and Conclusions

In this paper, a spatial ILC control framework was presented and validated. Through signature extraction and spatial registration methods, images from a high-speed NIR camera were used to implement a spatial ILC algorithm. The proposed framework demonstrated spatial registration capabilities from asynchronous camera measurements, and showed that the spatial ILC algorithm can reduce geometry-dependent inhomogeneities that occur at turnaround points on the edges. Four squares of 30 layers were fabricated, one with a constant laser power and three with the spatial ILC algorithm using different gains. The controllers all regulated the internal and edge points to the reference melt pool area value while using a constant laser power resulted in different melt pool area sizes in different regions. The standard deviation was lowest for the controller with $\gamma = 1$, similar for the open-loop and controller with $\gamma = 0.04$, and largest for the controller with $\gamma = 4$. The controller with $\gamma = 0.04$ did not reject disturbances on the edges, and the controller with $\gamma = 4$ amplified process noise making the standard deviation very large. The results show that the spatial registration and spatial ILC algorithm together can regulate the melt pool area with low variation over the entire part geometry.

References

- [1] Wohlers, T. (2014). Wohlers report. Wohlers Associates Inc.
- [2] Haghdadi, N., Laleh, M., Moyle, M., & Primig, S. (2021). Additive manufacturing of steels: a review of achievements and challenges. *Journal of Materials Science*, 56(1), 64-107.
- [3] Everton, S. K., Hirsch, M., Stravroulakis, P., Leach, R. K., & Clare, A. T. (2016). Review of in-situ process monitoring and in-situ metrology for metal additive manufacturing. *Materials & Design*, 95, 431-445.
- [4] Berumen, S., Bechmann, F., Lindner, S., Kruth, J. P., & Craeghs, T. (2010). Quality control of laser-and powder bed-based Additive Manufacturing (AM) technologies. *Physics procedia*, 5, 617-622.
- [5] Kruth, J. P., Mercelis, P., Van Vaerenbergh, J., & Craeghs, T. (2007). Feedback control of selective laser melting. In *Virtual and Rapid Manufacturing* (pp. 521-528). Crc Press.
- [6] Clijsters, Stijn, Tom Craeghs, Sam Buls, Karolien Kempen, and J-P. Kruth. "In situ quality control of the selective laser melting process using a high-speed, real-time melt pool monitoring system." *The International Journal of Advanced Manufacturing Technology* 75, no. 5 (2014): 1089-1101.
- [7] Craeghs, T., Bechmann, F., Berumen, S., & Kruth, J. P. (2010). Feedback control of Layerwise Laser Melting using optical sensors. *Physics Procedia*, 5, 505-514.
- [8] Schwerdtfeger, J., Singer, R. F., & Körner, C. (2012). In situ flaw detection by IR-imaging during electron beam melting. *Rapid Prototyping Journal*.
- [9] Gökhan Demir, A., De Giorgi, C., & Previtali, B. (2018). Design and implementation of a multisensor coaxial monitoring system with correction strategies for selective laser melting of a maraging steel. *Journal of Manufacturing Science and Engineering*, 140(4).
- [10] Shkoruta, A., Caynoski, W., Mishra, S., & Rock, S. (2019, August). Iterative learning control for power profile shaping in selective laser melting. In *2019 IEEE 15th International Conference on Automation Science and Engineering (CASE)* (pp. 655-660). IEEE.
- [11] Shkoruta, A., Mishra, S., & Rock, S. (2020, July). An experimental study on process modeling for selective laser melting. In *2020 American Control Conference (ACC)* (pp. 467-473). IEEE.
- [12] Krauss, H., Zeugner, T., & Zaeh, M. F. (2014). Layerwise monitoring of the selective laser melting process by thermography. *Physics Procedia*, 56, 64-71.
- [13] Krauss, H., Zeugner, T., & Zaeh, M. F. (2015, March). Thermographic process monitoring in powderbed based additive manufacturing. In *AIP Conference Proceedings* (Vol. 1650, No. 1, pp. 177-183). American Institute of Physics.
- [14] Lough, C. S., Wang, X., Smith, C. C., Landers, R. G., Bristow, D. A., Drallmeier, J. A., ... & Kinzel, E. C. (2020). Correlation of SWIR imaging with LPBF 304L stainless steel part properties. *Additive Manufacturing*, 35, 101359.
- [15] Lough, C. S., Wang, X., Smith, C. C., Adeniji, O., Landers, R. G., Bristow, D. A., & Kinzel, E. C. (2018). Use of SWIR imaging to monitor layer-to-layer part quality during SLM of 304l stainless steel.